



ALMA MATER STUDIORUM  
UNIVERSITÀ DI BOLOGNA

## ARCHIVIO ISTITUZIONALE DELLA RICERCA

### Alma Mater Studiorum Università di Bologna Archivio istituzionale della ricerca

The effect of local thermal non-equilibrium on the onset of thermal instability for a metallic foam

This is the final peer-reviewed author's accepted manuscript (postprint) of the following publication:

*Published Version:*

The effect of local thermal non-equilibrium on the onset of thermal instability for a metallic foam / Romulo Bessi Freitas, Pedro Vayssiere Brandão, Leonardo Santos de Brito Alves, Michele Celli, Antonio Barletta. - In: PHYSICS OF FLUIDS. - ISSN 1070-6631. - STAMPA. - 34:3(2022), pp. 034105.1-034105.11. [10.1063/5.0083045]

*Availability:*

This version is available at: <https://hdl.handle.net/11585/880113> since: 2022-03-29

*Published:*

DOI: <http://doi.org/10.1063/5.0083045>

*Terms of use:*

Some rights reserved. The terms and conditions for the reuse of this version of the manuscript are specified in the publishing policy. For all terms of use and more information see the publisher's website.

This item was downloaded from IRIS Università di Bologna (<https://cris.unibo.it/>).  
When citing, please refer to the published version.

(Article begins on next page)

This is the final peer-reviewed accepted manuscript of:

**Rômulo Bessi Freitas, Pedro Vayssière Brandão, Leonardo Santos de Brito Alves, Michele Celli, Antonio Barletta; The effect of local thermal non-equilibrium on the onset of thermal instability for a metallic foam. *Physics of Fluids* 1 March 2022; 34 (3): 034105**

The final published version is available online at:

<https://doi.org/10.1063/5.0083045>

Terms of use:

Some rights reserved. The terms and conditions for the reuse of this version of the manuscript are specified in the publishing policy. For all terms of use and more information see the publisher's website.

This item was downloaded from IRIS Università di Bologna (<https://cris.unibo.it/>)

**When citing, please refer to the published version.**

1 **The effect of local thermal non-equilibrium on the onset of thermal instability for a**  
2 **metallic foam**

3 Rômulo Bessi Freitas,<sup>1,2</sup> Pedro Vayssière Brandão,<sup>3</sup> Leonardo Santos de Brito Alves,<sup>2, a)</sup>  
4 Michele Celli,<sup>3</sup> and Antonio Barletta<sup>3</sup>

5 <sup>1</sup>*CODIB, CEFET/RJ, Estrada de Adrianópolis, 1.317, Santa Rita, Nova Iguaçu,*  
6 *RJ 26041-271, Brazil*

7 <sup>2</sup>*PGMEC, UFF, Rua Passo da Pátria 156, Bloco E, Sala 211, Niterói,*  
8 *Rio de Janeiro 24210-240, Brazil*

9 <sup>3</sup>*DIE, Alma Mater Studiorum Università di Bologna, Viale Risorgimento 2,*  
10 *40136 Bologna, Italy*

11 (Dated: 4 February 2022)

12 Mixed convection in metallic foams modeled with Darcy's law under local thermal non-  
13 equilibrium conditions is investigated, where the solid phase thermal conductivity is as-  
14 sumed infinitely larger than its fluid phase's counterpart. A linear and modal stability anal-  
15 ysis was employed to evaluate the convective and absolute instability thresholds as well  
16 as their respective cell patterns. This analysis indicates that local thermal non-equilibrium  
17 always has a stabilizing effect and the spanwise uniform mode is always the most unstable.  
18 At the onset of convective instability, however, the number of equally unstable cell patterns  
19 increases with both aspect ratio and local thermal non-equilibrium strength.

---

<sup>a)</sup>Electronic mail: lsbalves@id.uff.br

## 20 I. INTRODUCTION

21 In the last decades, there has been an increasing interest in the use of metallic foams as heat  
22 exchangers. This type of material is characterized especially by its stiffness, strength, lightness  
23 and ability to absorb a large amount of energy. The importance of this kind of material to heat  
24 transfer enhancement is mainly due to its high thermal conductivity, its high solid–fluid interface  
25 area and its ability to promote mixing internally<sup>1</sup>. Metallic foams are often modeled as porous  
26 media with high porosity and permeability. In addition, on account of their good conducting solid  
27 phase compared to the fluid phase, the assumption of local thermal equilibrium between the phases  
28 is likely to fail. For a thorough review on metallic foams and their application as heat exchangers,  
29 we refer the reader to the existing literature<sup>2–4</sup>.

30 A good understanding of the phenomenon of convection in porous media is closely related to  
31 the design optimization of metal foams as heat exchangers. The study of thermal instability to  
32 determine the onset of convection in fluid saturated porous media has been widely investigated  
33 in the literature. The pioneering studies in this field<sup>5,6</sup> focused on a porous layer saturated by a  
34 Newtonian fluid at rest. Some years later, the effect of a horizontal fluid flow on the transition  
35 to instability was investigated<sup>7</sup>. It was found that the horizontal throughflow does not affect the  
36 instability threshold, but changes the disturbance nature from stationary to travelling.

37 These conclusions were based on the concept of convective stability analysis. Such an analysis  
38 aims to determine the parametric threshold above which a plane wave disturbance with a given  
39 wave number starts to grow. In the late 1950s, a discussion emerged between different types of  
40 instability in the context of plasma physics<sup>8,9</sup>. Later, the concepts of convective and absolute in-  
41 stabilities were brought to the area of fluid dynamics<sup>10</sup>. The distinction between these types of  
42 instability can be done by analyzing the impulse response of the system. If the infinitesimal im-  
43 pulse grows in time for a fixed position, eventually contaminating the entire domain, the problem  
44 is said to be absolutely unstable. On the other hand, if a disturbance grows as it is convected by  
45 the basic flow, eventually leaving the domain, it is said to be convectively unstable. If the problem  
46 has a basic solution in which the fluid is at rest, the onset conditions of both types of instability  
47 most likely coincide. When the basic throughflow is nonzero, however, which is the case in many  
48 real–world problems, the convective/absolute instability nature of the flow must be determined.

49 Recently, absolute instability in porous media flows has been the focus of several studies<sup>11–20</sup>,  
50 and a more exhaustive review can be found in Barletta<sup>21</sup>. In the context of convection within

51 metallic foams, the onset of absolute instability is yet an unanswered question. The present paper  
52 aims to investigate the transition from convective to absolute instability when the solid and fluid  
53 phases are not in local thermal equilibrium. The first studies on the onset of convective instability  
54 in a horizontal porous layer under conditions of local thermal non-equilibrium were carried out  
55 by Combarrous<sup>22</sup> and later by Banu and Rees<sup>23</sup>. In addition, we consider the porous channel to  
56 be laterally confined. The pattern selection of the emergent mixed convection is also investigated.  
57 This investigation is usually performed by means of a weakly nonlinear analysis, since the inter-  
58 action between the single modes must be taken into account<sup>24</sup>. Such an approach has indeed been  
59 used to investigate the effect of local thermal non-equilibrium on the pattern formation for mixed  
60 convection in porous media<sup>25</sup>. In the present analysis, however, only the linear pattern selection is  
61 discussed. This is accomplished by employing the linear growth rates given by both the convective  
62 and absolute instability analyses.

## 63 **II. PROBLEM STATEMENT**

64 A fluid saturated porous layer is bounded horizontally by impermeable and isothermal walls  
65 and vertically by adiabatic and impermeable walls. This porous channel is subject to a horizontal  
66 pressure gradient. A vertical temperature gradient is set up by imposing two different tempera-  
67 tures at the boundaries with the highest temperature on the lower one. The problem configuration  
68 is illustrated in the Fig. 1 and coincides with the one investigated by Prats, but with a lateral  
69 confinement. Among all the possible porous media, we are interested in investigating metallic  
70 foams. These peculiar, highly conductive, porous media are suitable for designing innovative  
71 heat exchangers. In this framework, heat transfer processes characterised by fast transients are  
72 frequent. In order to analyse this type of phenomena, a two-temperature model is here employed:  
73 one temperature describing the heat transfer for the fluid phase and one temperature for the heat  
74 transfer for the solid phase. This model allows us to relax the hypothesis of local thermal equilib-  
75 rium (LTE) between the solid phase and the fluid phase.

76

77 The stability of such a system with respect to the onset of buoyancy driven convection will  
78 be investigated in this paper. The convective stability and absolute instability are here studied.  
79 Darcy's law is employed to describe the momentum transfer and the Oberbeck-Boussinesq ap-  
80 proximation is assumed to model the buoyancy term.

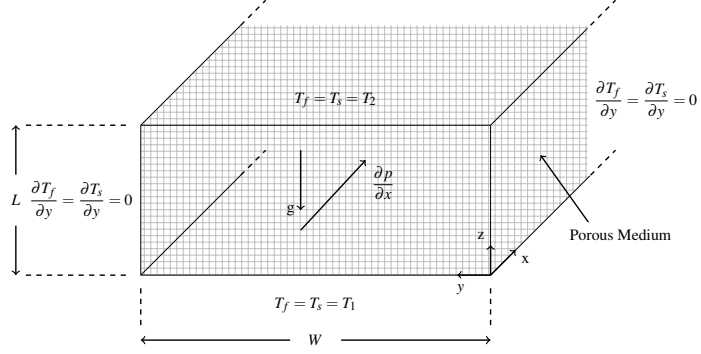


FIG. 1. Illustration of the flow geometry under study.

### 81 A. Governing equations

The absence of LTE implies a so called local thermal non equilibrium (LTNE) regime. The two-temperature model here employed defines, for the same reference elementary volume, two different temperatures and a interphase heat transfer coefficient  $h$  that rules the heat exchange between solid and fluid. The set of governing equations is thus composed by a local mass balance equation, a local momentum balance equation, and two energy balance equations, one for the fluid and one for the solid, namely

$$\begin{aligned}
 \nabla \cdot \mathbf{u} &= 0, \\
 \frac{\mu}{K} \mathbf{u} &= -\nabla p + \rho_f g \beta (T_f - T_0) \mathbf{e}_z, \\
 (\rho c)_f \left( \varphi \frac{\partial T_f}{\partial t} + \mathbf{u} \cdot \nabla T_f \right) &= \varphi k_f \nabla^2 T_f - h (T_f - T_s), \\
 (\rho c)_s (1 - \varphi) \frac{\partial T_s}{\partial t} &= (1 - \varphi) k_s \nabla^2 T_s + h (T_f - T_s), \\
 y = 0 : \quad \frac{\partial T_f}{\partial y} = \frac{\partial T_s}{\partial y} &= 0, \quad v = 0, \\
 y = W : \quad \frac{\partial T_f}{\partial y} = \frac{\partial T_s}{\partial y} &= 0, \quad v = 0, \\
 z = 0 : \quad T_f = T_s = T_1, \quad w &= 0, \\
 z = L : \quad T_f = T_s = T_2, \quad w &= 0.
 \end{aligned} \tag{1}$$

where the  $x$  coordinate direction is assumed homogeneous. Hence, boundary conditions are not required by a linear and modal stability analysis in this direction. Here, the subscripts  $f, s$  denote,

respectively, the fluid phase and solid phase properties,  $(x, y, z)$  are the Cartesian components of the position vector  $\mathbf{x}$ ,  $t$  is the time,  $\mathbf{u} = (u, v, w)$  is the velocity vector,  $T$  is the temperature,  $T_0$  is the reference temperature,  $\mathbf{e}_z$  is the unit vector along the vertical  $z$ -axis,  $\rho$  is the density,  $c$  is the heat capacity per unit mass,  $k$  is the thermal conductivity,  $\phi$  is the porosity,  $\mu$  is the dynamic viscosity,  $\beta$  is the thermal expansion coefficient of the fluid,  $K$  is the permeability,  $g$  is the modulus of the gravitational acceleration vector  $\mathbf{g}$ . The channel height is denoted with  $L$  while the width with  $W$ . Noting that  $\varkappa = k/(\rho c)$  is the thermal diffusivity, the relations

$$\begin{aligned} \mathbf{x} &= \mathbf{x}^* L, \quad t = t^* \frac{L^2}{\varkappa_f}, \quad \mathbf{u} = \mathbf{u}^* \frac{\phi \varkappa_f}{L}, \quad p = p^* \frac{\phi \mu \varkappa_f}{K}, \\ T_{s,f} &= T_0 + T_{s,f}^* \Delta T, \quad T_0 = \frac{T_1 + T_2}{2}, \quad \Delta T = T_1 - T_2, \end{aligned} \quad (2)$$

yield the definitions of the dimensionless quantities, denoted with an asterisk. Eq. (2) allows us to obtain the following set of dimensionless governing equations from Eq. (1):

$$\begin{aligned} \nabla \cdot \mathbf{u} &= 0, \\ \mathbf{u} &= -\nabla p + RT_f \mathbf{e}_z, \\ \frac{\partial T_f}{\partial t} + \mathbf{u} \cdot \nabla T_f &= \nabla^2 T_f - H(T_f - T_s), \\ \xi \frac{\partial T_s}{\partial t} &= \nabla^2 T_s + H\gamma(T_f - T_s), \\ y = 0, A: \quad \frac{\partial T_f}{\partial y} = \frac{\partial T_s}{\partial y} &= 0, \quad v = 0, \\ z = 0, 1: \quad T_f = T_s &= \pm \frac{1}{2}, \quad w = 0, \end{aligned} \quad (3)$$

where the asterisks are omitted for the sake of brevity and the forthcoming analysis is based on dimensionless quantities. The Darcy–Rayleigh number  $R$  and the other dimensionless parameters employed in Eqs. (3) are defined as

$$\xi = \frac{\varkappa_f}{\varkappa_s}, \quad H = \frac{hL^2}{\phi k_f}, \quad \gamma = \frac{\phi k_f}{(1-\phi)k_s}, \quad R = \frac{g\beta\Delta T K L}{\phi \varkappa_f \nu}, \quad A = \frac{W}{L}. \quad (4)$$

## 82 B. Pressure–temperature formulation

We manipulate Eqs. (3) to obtain the following pressure temperature formulation

$$\begin{aligned}
& \nabla^2 p - R \frac{\partial T_f}{\partial z} = 0, \\
& \frac{\partial T_f}{\partial t} + (RT_f \mathbf{e}_z - \nabla p) \cdot \nabla T_f = \nabla^2 T_f - H(T_f - T_s), \\
& \xi \frac{\partial T_s}{\partial t} = \nabla^2 T_s + H \gamma (T_f - T_s), \\
& y = 0, A : \quad \frac{\partial T_f}{\partial y} = \frac{\partial T_s}{\partial y} = 0, \quad \frac{\partial p}{\partial y} = 0, \\
& z = 0, 1 : \quad T_f = T_s = \pm \frac{1}{2}, \quad \frac{\partial p}{\partial z} = \pm \frac{R}{2},
\end{aligned} \tag{5}$$

83 where the impermeability conditions in Eq. (3) are expressed as pressure conditions by employing  
84 Darcy's law.

## 85 III. STABILITY ANALYSIS

A metallic foam is usually characterized by a high value of thermal conductivity. Let us consider the limiting case where the fluid saturated metallic foam is such that  $k_f/k_s \ll 1$  with a finite value of  $k_f$ . This assumption yields  $\gamma \ll 1$  and  $\xi \ll 1$ . Such results yield an important simplification of Eqs. (5), namely

$$\begin{aligned}
& \nabla^2 p - R \frac{\partial T_f}{\partial z} = 0, \\
& \frac{\partial T_f}{\partial t} + (RT_f \mathbf{e}_z - \nabla p) \cdot \nabla T_f = \nabla^2 T_f - H(T_f - T_s), \\
& \nabla^2 T_s = 0, \\
& y = 0, A : \quad \frac{\partial T_f}{\partial y} = \frac{\partial T_s}{\partial y} = 0, \quad \frac{\partial p}{\partial y} = 0, \\
& z = 0, 1 : \quad T_f = T_s = \pm \frac{1}{2}, \quad \frac{\partial p}{\partial z} = \pm \frac{R}{2}.
\end{aligned} \tag{6}$$

## 86 A. The basic state

A stationary basic solution of Eq. (3) where a horizontal pressure gradient is imposed is the following:

$$\nabla p_b = (-Pe, 0, RT_{f,b}), \quad T_{s,b} = T_{f,b} = \frac{1}{2} - z, \tag{7}$$



87 where  $b$  stands for the basic state and  $Pe = u_0 L / \varphi \varkappa_f$  is the Péclet number, which derives from  
 88 the velocity scaling in Eq. (2) with  $u_0$  defined as characteristic velocity imposed by the stationary  
 89 pressure gradient. Since the temperatures of the fluid and of the solid phase coincide, the basic  
 90 state is one of local thermal equilibrium.

## 91 B. Linear and modal disturbance governing equations

The stability of the basic state, Eqs. (7), is now investigated. The governing equations (6) are thus perturbed by employing small amplitude disturbances, namely

$$\begin{pmatrix} p(x, y, z, t) \\ T_f(x, y, z, t) \\ T_s(x, y, z, t) \end{pmatrix} = \begin{pmatrix} p_b(x, z) \\ T_{f,b}(z) \\ T_{s,b}(z) \end{pmatrix} + \varepsilon \begin{pmatrix} p_d(x, y, z, t) \\ T_{f,d}(x, y, z, t) \\ T_{s,d}(x, y, z, t) \end{pmatrix}, \quad (8)$$

where  $d$  stands for the disturbance and  $\varepsilon$  is a disturbance parameter, small enough to make the  $O(\varepsilon^2)$  nonlinear terms negligible. The linearised system of governing equations obtained by substituting Eq. (8) into Eqs. (6):

$$\nabla^2 p_d - R \frac{\partial T_{f,d}}{\partial z} = 0, \quad (9a)$$

$$\frac{\partial T_{f,d}}{\partial t} + Pe \frac{\partial T_{f,d}}{\partial x} + \frac{\partial p_d}{\partial z} - R T_{f,d} = \nabla^2 T_{f,d} - H(T_{f,d} - T_{s,d}), \quad (9b)$$

$$\nabla^2 T_{s,d} = 0, \quad (9c)$$

$$y = 0, A : \quad \frac{\partial T_{f,d}}{\partial y} = \frac{\partial T_{s,d}}{\partial y} = \frac{\partial p_d}{\partial y} = 0, \quad (9d)$$

$$z = 0, 1 : \quad T_{f,d} = T_{s,d} = 0, \quad \frac{\partial p_d}{\partial z} = 0. \quad (9e)$$

We can now express  $(p_d, T_{f,d}, T_{s,d})$  in terms of the Fourier modes

$$\begin{aligned} p_d &= \frac{1}{\sqrt{2\pi}} \int_{-\infty}^{+\infty} \psi(y, z) e^{ikx} e^{\lambda t} dk, \\ T_{f,d} &= \frac{1}{\sqrt{2\pi}} \int_{-\infty}^{+\infty} \theta(y, z) e^{ikx} e^{\lambda t} dk, \\ T_{s,d} &= \frac{1}{\sqrt{2\pi}} \int_{-\infty}^{+\infty} \phi(y, z) e^{ikx} e^{\lambda t} dk, \end{aligned} \quad (10)$$

which are spatially periodic and temporally evolving since  $k$  is a real wave number and  $\lambda$  is a complex parameter with frequency  $\omega = -Im[\lambda]$  and temporal growth rate  $Re[\lambda]$ . Alternatively,

they can also be expressed in terms of the Fourier modes

$$\begin{aligned} p_d &= \frac{1}{\sqrt{2\pi}} \int_{-\infty}^{+\infty} \psi(y, z) e^{ikx} e^{-i\omega t} d\omega, \\ T_{f,d} &= \frac{1}{\sqrt{2\pi}} \int_{-\infty}^{+\infty} \theta(y, z) e^{ikx} e^{-i\omega t} d\omega, \\ T_{s,d} &= \frac{1}{\sqrt{2\pi}} \int_{-\infty}^{+\infty} \phi(y, z) e^{ikx} e^{-i\omega t} d\omega, \end{aligned} \quad (11)$$

which are temporally periodic and spatially evolving since  $\omega$  is a real frequency and  $k$  is a complex parameter with wave number  $Re[k]$  and spatial growth rate  $-Im[k]$ . Furthermore, they also have complex eigenfunctions  $\psi(y, z)$ ,  $\theta(y, z)$  and  $\phi(y, z)$  that depend on the parameters  $k$  and  $n$  or  $\omega$  and  $n$ , respectively. By employing Eq. (10), we can manipulate Eq. (9) to obtain

$$\begin{aligned} \frac{\partial^2 \psi}{\partial y^2} + \frac{\partial^2 \psi}{\partial z^2} - k^2 \psi - R \frac{\partial \theta}{\partial z} &= 0, \\ \frac{\partial^2 \theta}{\partial y^2} + \frac{\partial^2 \theta}{\partial z^2} - (k^2 + H - R + ikPe + \lambda) \theta - \frac{\partial \psi}{\partial z} + H\phi &= 0, \\ \frac{\partial^2 \phi}{\partial y^2} + \frac{\partial^2 \phi}{\partial z^2} - k^2 \phi &= 0, \\ y = 0, A: \quad \frac{\partial \theta}{\partial y} = \frac{\partial \phi}{\partial y} = \frac{\partial \psi}{\partial y} &= 0, \\ z = 0, 1: \quad \theta = \phi = 0, \quad \frac{\partial \psi}{\partial z} &= 0, \end{aligned} \quad (12)$$

which can also be obtained from Eq. (11) if we let  $\omega = i\lambda$ . The disturbances  $(\psi, \theta, \phi)$  can be expressed in the form of normal modes according to the boundary conditions in Eq. (14)

$$\begin{aligned} \psi &= \sum_{n=0}^{\infty} \sum_{m=1}^{\infty} \psi_{n,m} \cos\left(\frac{n\pi y}{A}\right) \cos(m\pi z), \\ \theta &= \sum_{n=0}^{\infty} \sum_{m=1}^{\infty} \theta_{n,m} \cos\left(\frac{n\pi y}{A}\right) \sin(m\pi z), \\ \phi &= \sum_{n=0}^{\infty} \sum_{m=1}^{\infty} \phi_{n,m} \cos\left(\frac{n\pi y}{A}\right) \sin(m\pi z). \end{aligned} \quad (13)$$

By applying Eq. (13) to Eq. (12) we may write

$$\begin{aligned} (k^2 + s^2 + \pi^2 m^2) \psi_{n,m} + \pi m R \theta_{n,m} &= 0, \\ (\lambda + k^2 + s^2 + ikPe + \pi^2 m^2 - R) \theta_{n,m} - \pi m \psi_{n,m} + H(\theta_{n,m} - \phi_{n,m}) &= 0, \\ (k^2 + \pi^2 m^2 + s^2) \phi_{n,m} &= 0, \end{aligned} \quad (14)$$

where

$$s^2 = \frac{n^2 \pi^2}{A^2}. \quad (15)$$

The last equation in Eqs. (14) allows us to conclude that  $\phi_{n,m} = 0$  for every  $n$  and  $m$ , which means its first two equations can be manipulated to yield the dispersion relation

$$\lambda = R - \frac{\pi^2 m^2 R}{k^2 + \pi^2 m^2 + s^2} - H - k^2 - s^2 - \pi^2 m^2 - ik Pe. \quad (16)$$

With the aim of encompassing the dependence on  $m$ , we introduce the scaling

$$\lambda' = \frac{\lambda}{m^2}, \quad R' = \frac{R}{m^2}, \quad H' = \frac{H}{m^2}, \quad k' = \frac{k}{m}, \quad s' = \frac{s}{m}, \quad Pe' = \frac{Pe}{m}, \quad (17)$$

so that Eq. (16) can be rewritten as

$$\lambda' = R' - \frac{\pi^2 R'}{k'^2 + \pi^2 + s'^2} - H' - k'^2 - s'^2 - \pi^2 - ik' Pe'. \quad (18)$$

Equation (18) coincides with Eq. (16) when  $m = 1$ . In the following, the primes will be omitted for the sake of brevity. This is equivalent to employing Eq. (16) with  $m = 1$ .

### C. Onset of convective instability

The first step in the present study is to identify the onset of instability, i.e. under which parametric conditions the flow first becomes unstable. In the presence of throughflow, this is often called the onset of convective instability. This analysis can be pursued by considering either spatially periodic Fourier modes that can neither grow nor decay in time, i.e.  $Re[\lambda] = 0$ , or temporally periodic Fourier modes that neither grow nor decay in space, i.e.  $-Im[k] = 0$ .

Under these constraints, the imaginary part of Eq. (18) yields

$$\omega = k Pe. \quad (19)$$

This result implies that traveling disturbances propagate at the same dimensionless velocity of the basic flow, Eq. (7). We can thus conclude that the principle of exchange of stabilities holds in the reference frame co-moving with the basic flow.

Putting together Eq. (19) with the assumptions  $Im[k] = Re[\lambda] = 0$  and Eq. (18), yields

$$R = \frac{(k^2 + s^2 + \pi^2)(k^2 + s^2 + H + \pi^2)}{k^2 + s^2}, \quad (20)$$

where the least stable mode is recovered when  $m = 1$  according to Eq. (17). The critical values  $k_c$ , which are the values of  $k$  that minimize  $R$ , must satisfy either equation

$$\begin{cases} k^2 + s^2 = s_c^2 & \forall s \leq s_c, \\ k = 0 & \forall s, \end{cases} \quad (21)$$

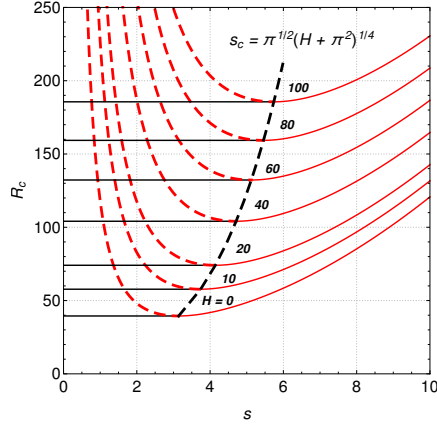


FIG. 2. Critical Rayleigh number  $R_c$  as a function of the parameter  $s$  for different values of  $H$ . Black lines represent  $R_c \forall s \leq s_c$  whereas red lines represent  $R_c \forall s$  in Eq. (23). Dashed (red) line represents local minima whereas solid (black and red) lines represent global minima.

where the former describes a circle centered at the origin  $(k, s) = (0, 0)$  with radius  $s_c$ , defined as

$$s_c = \sqrt{\pi}(H + \pi^2)^{1/4}. \quad (22)$$

They represent the wave number of the disturbance that will first become unstable as  $R$  is increased to  $R_c = R(k_c)$ . Substituting Eq. (21) into Eq. (20) leads to the critical Rayleigh numbers

$$R_c = \begin{cases} H + 2\pi(\pi + \sqrt{H + \pi^2}) & \forall s \leq s_c, \\ \frac{(\pi^2 + s^2)(H + \pi^2 + s^2)}{s^2} & \forall s, \end{cases} \quad (23)$$

which show that the parameter  $R_c$  has a dependency on both  $s$  and  $H$ . Figure 2 summarizes these findings by presenting  $R_c$  from Eq. (23) as a function of  $s$  for different  $H$ . Note that  $s_c$  increases as  $H$  increases, which is why the critical interval increases with  $H$ . Since  $R_c(\forall s \leq s_c) \leq R_c(\forall s)$ , as shown in Fig. 2, and  $s \leq s_c$ , because the integer  $n$  can be as small as zero as it was defined in Eq. (13), the critical wavelength is given by  $k_c = \sqrt{s_c^2 - s^2}$ . Two limits are worth further discussion. One is the unlikely upper limit  $s = s_c$ , since it can only be achieved when  $A$  and  $n$  satisfy

$$A = n\sqrt{\pi}/(H + \pi^2)^{1/4}, \quad (24)$$

which means that we must have  $A = n$  when  $H = 0$  and  $A = n/2$  when  $H = 15\pi^2$ , for instance. In these very specific cases, a uniform ( $k_c = 0$ ) and stationary ( $\omega_c = 0$ ), according to Eq. (19), disturbance becomes dominant. The other one is the lower limit  $s \rightarrow 0$  for either an unbounded domain in the streamwise direction, i.e.  $A \rightarrow \infty$ , or a spanwise uniform instability, i.e.  $n = 0$ . Equation (20) can then be simplified to

$$k_c = \sqrt{\pi\sqrt{H + \pi^2}}. \quad (25)$$

103 Furthermore, the thermal uncoupling between solid and fluid phases occurs for a vanishing dimen-  
 104 sionless inter-phase heat transfer coefficient, i.e. in the limit  $H \rightarrow 0$ . In this case, if  $s \rightarrow 0$ , the  
 105 mathematical formulation matches that of the classical Darcy–Bénard problem and one obtains  
 106  $k_c = \pi$  from Eq. (25) and  $R_c = 4\pi^2$  from Eq. (23). Finally, it is important to note that the classical  
 107 Darcy–Bénard Rayleigh number  $Ra$  and the one used here are not the same. According to Eq. (4),  
 108 they are related by  $Ra = \gamma R / (1 + \gamma)$ . Additionally,  $\gamma \rightarrow 0$  because  $k_s \gg k_f$  was assumed and  
 109 Eq. (23) states that  $R_c \rightarrow \infty$  as  $H \rightarrow \infty$ . Hence, both products  $\gamma R$  and  $\gamma H$  become ill-defined when  
 110  $H \rightarrow \infty$ . The latter also appears in Eq. (5), which means this limit cannot be enforced when using  
 111 Eq. (6). It turns out that  $\gamma \sim O(10^{-3})$  and  $O(1) < H < O(10^5)$ , according to typical values found  
 112 in the literature for  $h, L, \varphi, k_s$  and  $k_f$ <sup>1</sup>. Hence, we focus our studies on the range  $0 \leq H \leq 100$ .

#### 113 D. Onset of absolute instability

The onset of convective instability can be analyzed by studying the first Fourier mode that becomes unstable. The onset of absolute instability, on the other hand, requires an analysis of the entire convectively unstable wavepacket. It occurs when the upstream edge of this wavepacket becomes stationary. This can be numerically evaluated through the zero group velocity condition

$$\frac{\partial \lambda}{\partial k} = 0, \quad (26)$$

which marks the location of the saddle point  $\{k_0, \lambda(k_0)\}$ . The steepest descent calculation required to pursue this analysis extends the real wave number  $k$  of spatially periodic Fourier modes into the complex plane, allowing it to be complex. By employing Eq. (16) and the zero group velocity condition (26), the saddle points  $k_0$  must be evaluated numerically by using a root finding procedure. The Rayleigh number at the saddle point,  $R_0 = R(k_0, \lambda(k_0))$ , is obtained by evaluating

$$Re[\lambda(k_0)] = 0. \quad (27)$$

114 Since Eq. (26) is a necessary but not sufficient condition for absolute instability, causality must be  
 115 verified to make sure that the Rayleigh number at the onset of absolute instability  $R_a$  is equal to  $R_0$ .  
 116 This is done for a large enough number of saddle points in order to generate enough confidence  
 117 that the entire set satisfies causality. A sample case is presented in Fig. 3 for  $H = 10$ ,  $Pe = 10$  and  
 118  $s = 2$ . Causality is demonstrated in two different ways. One is a simple visual inspection to make  
 119 sure that the downstream propagating branch, labeled  $k^+$ , goes from stable ( $R < R_c$ ) to marginally  
 120 stable ( $R = R_c$ ) to convectively unstable ( $R_c < R < R_a$ ) to marginally absolutely stable ( $R = R_a$ ),  
 121 at which point it pinches with a stable upstream propagating branch, labeled  $k^-$ . Another way is  
 122 by calculating the steepest descent curve, shown by the red dashed line in Fig. 3 (left), in order to  
 123 demonstrate that it contains no singularity. The steepest ascent curve, shown by the blue dashed  
 124 line in Fig. 3 (left), yields the wave packet characteristic group velocity shown in Fig. 3 (right).

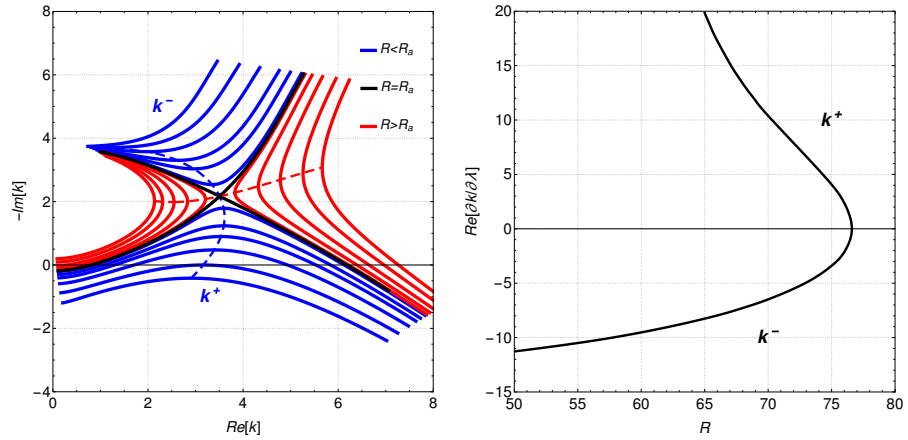


FIG. 3. Stability branches for  $H = 10$ ,  $Pe = 10$  and  $s = 2$ . (Left) Collision criterion together with steepest ascent (blue) and descent (red) paths passing through the saddle point. (Right) Characteristic group velocity of both wave packets involved in the collision at the saddle point.

125 Once we gained confidence that these calculations indeed yielded onsets of absolute instability,  
 126 a parametric analysis was pursued. The value of  $R_a$  as a function of  $s$  for a range of Péclet numbers  
 127 is shown in Fig. 4 with (left)  $H = 0$  and (right)  $H = 10$ . When  $Pe = 0$ , the onsets of convective and  
 128 absolute instability occur at the same threshold Rayleigh number, i.e.  $R_c = R_a$ . Otherwise, a region  
 129 of convective instability appears when  $Pe > 0$ . Furthermore, for a given value of  $s$ , increasing either

130  $Pe$  or  $H$  has a stabilizing effect, i.e.  $R_a$  increases. Although Fig. 4 clearly shows this stabilizing  
 131 effect of  $Pe$ , the same cannot be said about  $H$ . In order to highlight the effect of thermal non-  
 132 equilibrium, the threshold (top left) Darcy–Rayleigh number, (top right) frequency, (bottom left)  
 133 spatial growth rate and (bottom right) wave number at the onset of absolute instability are shown  
 134 as functions of  $H$  for different  $Pe$  in Fig. 5 when  $s = 0$ . This value of  $s$  was selected because Fig. 4  
 135 shows that it yields the location of all global minima when the Péclet number is positive. The  
 136 stabilizing effect of  $H$  is now clearly shown in Fig. 5. Furthermore, both threshold frequency and  
 137 wave number increase with  $H$ . These trends are the same for any positive Péclet number. On the  
 138 other hand, the qualitative impact of  $H$  on the spatial growth rate depends on the Péclet number.  
 139 For small (large)  $Pe$ , the spatial growth rate decreases (increases) when  $H$  increases.

#### 140 IV. LINEAR PATTERN SELECTION

141 As discussed in section III C, the onset of convective instability occurs for an infinite combina-  
 142 tion of aspect ratios  $A$  and Fourier modes  $n$ , which indicates the spanwise cell pattern. Figure 6  
 143 highlights this issue by showing the critical (left) Rayleigh number and (right) wave number as  
 144 functions  $A$  for different  $n$  when  $H = 0$ . This figure shows the cell pattern selected at the onset

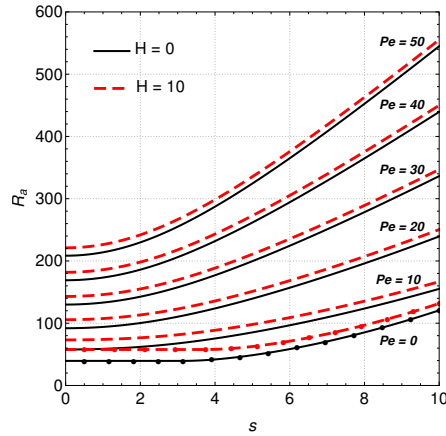


FIG. 4. Critical Rayleigh numbers as function of  $s$  representing the onsets of convective (dots) and absolute (lines) instability for a range of Péclet numbers with (black solid)  $H = 0$  and (red dashed)  $H = 10$ .

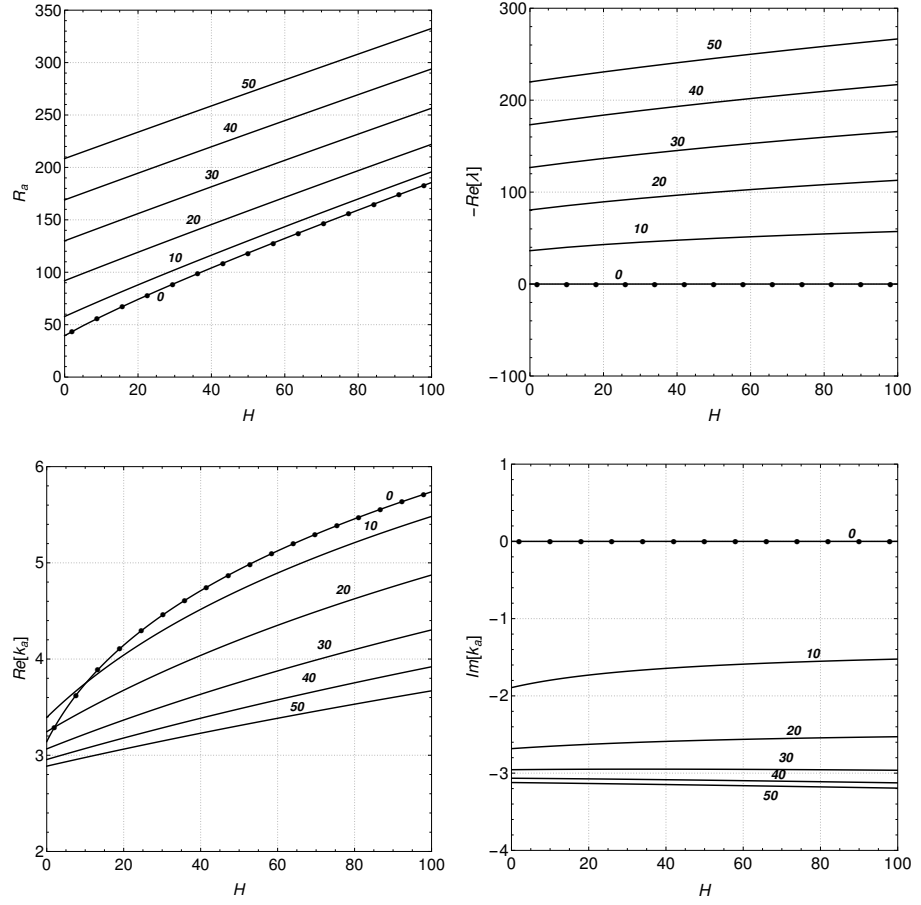


FIG. 5. Critical (top left) Darcy–Rayleigh number, (top right) frequency, (bottom left) spatial growth rate and (bottom right) wave number at the onset of absolute instability as functions of  $H$  for different  $Pe$  when  $s = 0$ .

145 of convective instability as a function of the aspect ratio in the regime of complete thermal un-  
 146 coupling between the phases. It is important to emphasize that the number of marginally unstable  
 147 patterns increases with  $A$ , indicating co-dimension points (black dots). They can be found by  
 148 equating both formulas for  $R_c$  in Eq. (23). In other words, Fig. 6 (left) shows that  $n = 0$  is the  
 149 only marginally unstable mode when  $A < 1$ , both  $n = 0$  and 1 modes are marginally unstable when



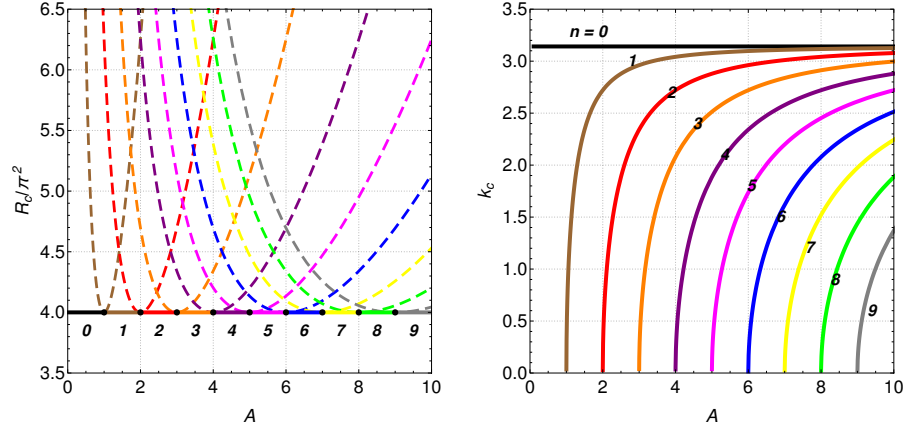


FIG. 6. Critical (left) Rayleigh number and (right) wave number at the onset of convective instability as functions of the aspect ratio for different Fourier modes when  $H = 0$ . Each color corresponds to a unique spanwise cell pattern  $n$ . Black dots indicate co-dimension points. Solid lines indicate that  $s \leq s_c$  whereas the dashed ones indicate that  $s \geq s_c$ , where  $s_c$  is defined in Eq. (22).

150  $A < 2$ , all three  $n = 0, 1$  and  $2$  modes are marginally unstable when  $A < 3$ , and so on. Furthermore,  
 151 Fig. 6 (right) shows that the critical wave number of each positive mode ( $n > 0$ ) increases with  $A$ ,  
 152 eventually reaching its asymptotic limit of  $k_c(A \rightarrow \infty) \rightarrow \pi$ , where  $k_c(\forall A) = \pi$  when  $n = 0$ . The  
 153 effect of thermal non-equilibrium on the marginally stable cell pattern formation can be evaluated  
 154 now by considering different values of  $H$ . These results are summarized in Fig. 7, which is similar  
 155 to Fig. 6 (left) but constrained to  $s \leq s_c$  and  $n < 10$ . By increasing  $H$  for a fixed  $A$  leads to an  
 156 increase in the number of unstable spanwise cell patterns. In other words, the co-dimension points  
 157 occur at smaller aspect ratios as  $H$  increases.

158 The identification of the cell patterns beyond marginal stability often requires a nonlinear anal-  
 159 ysis<sup>26</sup>. This is, however, beyond the scope of the present paper. Nonetheless, there is still much to  
 160 explore in this realm from a linear standpoint by distinguishing between convective and absolute  
 161 instabilities. Although they have been understood for decades now<sup>27</sup>, novel techniques for their  
 162 detection are still being developed<sup>28</sup> and their influence on porous media flows is still being un-  
 163 covered<sup>29</sup>. Figure 8 shows the most relevant Fourier modes (top left) at marginal stability, (top  
 164 right) during convective instability, (bottom left) at the onset of absolute instability as well as (bot-

165 tom right) during absolute instability for  $Pe = 10$ ,  $H = 30$  and  $A = 2.5$ . The first plot confirms  
 166 the information already discussed in Fig. 7, which showed that modes  $n = 0, 1, 2$  and  $3$  become  
 167 marginally unstable ( $\text{Re}[\lambda] = \text{Im}[k] = 0$ ) simultaneously at  $R = R_c$ . A convectively unstable re-  
 168 gion is reached beyond this point, i.e. when  $R_c < R < R_a$ , which means incoming disturbances are  
 169 spatially amplified ( $-\text{Im}[k] > 0$ ). In other words, they grow in amplitude as they are convected  
 170 downstream. Figure 8 (top right) shows that the spanwise uniform mode ( $n = 0$ ) has the highest  
 171 spatial growth rate when  $R = R_c + 10$ , which is in fact true for all convectively unstable conditions  
 172 evaluated. Assuming all incoming disturbances enter the flow with similar amplitudes, the  $n = 0$   
 173 mode is the most likely one to grow (in space) downstream and reach nonlinear saturation first.  
 174 The onset of absolute instability is then reached when  $R = R_a$  ( $\text{Re}[\lambda_a] = 0$ ). Beyond this point,  
 175 i.e. when  $R > R_a$ , disturbance measured at any given spatial location are temporally amplified  
 176 ( $\text{Re}[\lambda_a] > 0$ ). Saddle points shown in Fig. 8 (bottom left) indicate that the  $n = 0$  mode is the first  
 177 one to become absolutely unstable whereas the cusp points<sup>30</sup> shown in Fig. 8 (bottom right) indi-  
 178 cate that this same mode remains the dominant one within the absolutely unstable region. This is  
 179 true for all absolutely unstable onsets and absolutely unstable regions evaluated. Assuming that  
 180 all disturbances initially present in the flow have similar amplitudes, the  $n = 0$  mode is the most  
 181 likely one to grow (in time) and reach nonlinear saturation first. It should be emphasized again  
 182 that these are linear cell pattern selection mechanisms. Nonlinear interactions can change the cell

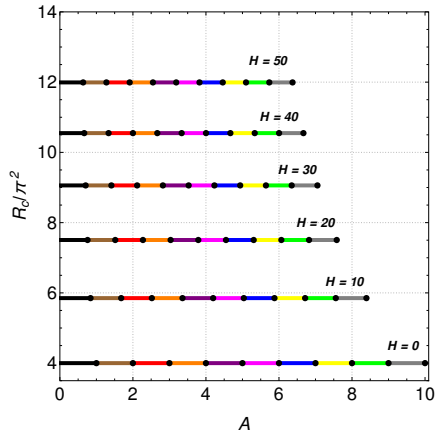


FIG. 7. Same as Fig. 6 (left), but for different positive  $H$  and constrained to  $n < 10$ .

183 pattern selected by the flow.

184 The linear spanwise cell pattern that is selected at the onset of absolute instability can now be  
 185 investigated a bit further. This is done here for  $Pe = 10$  and  $H = 30$ , although similar trends were  
 186 observed at all other parametric conditions evaluated. Figure 9 shows the critical (top left) Darcy–  
 187 Rayleigh number, (top right) frequency, (bottom left) spatial growth rate and (bottom right) wave  
 188 number at the onset of absolute instability as functions of the aspect ratio for the first ten Fourier

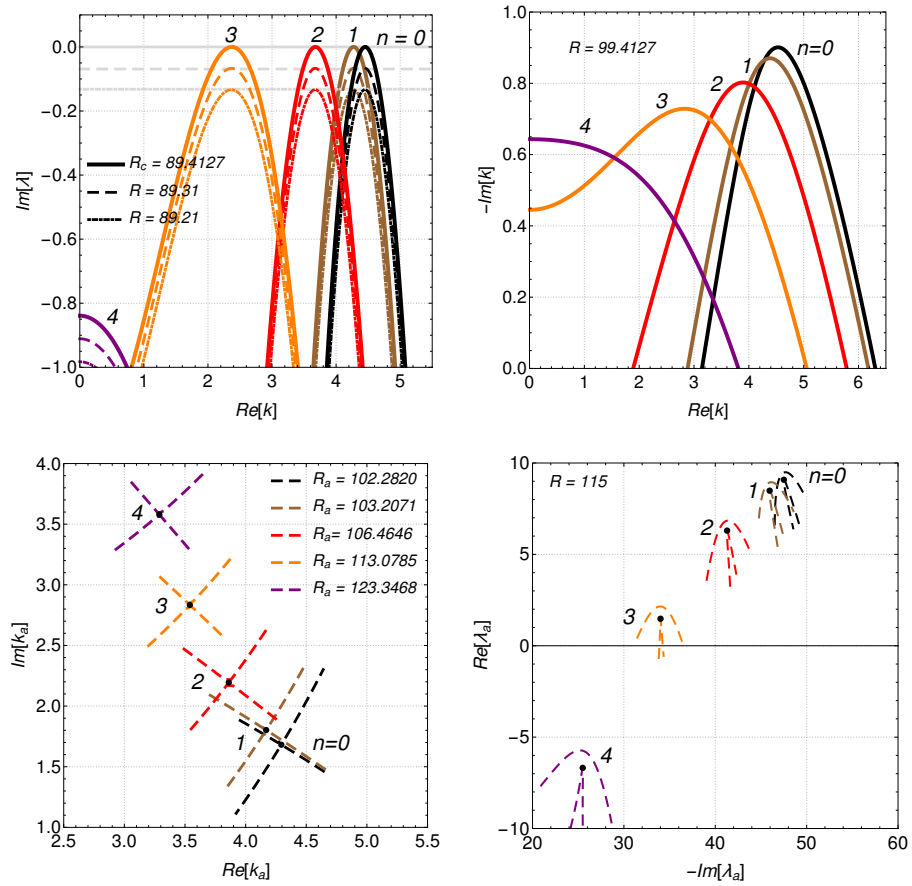


FIG. 8. Dominant spanwise cell patterns (top left) at marginal stability, (top right) during convective instability with  $R = R_c + 10$  and (bottom) at the onset of absolute instability for  $Pe = 10$ ,  $H = 30$  and  $A = 2.5$ .

189 modes. The spanwise uniform mode ( $n = 0$ ) is the first one to become absolutely unstable and this  
 190 onset is not affected by the aspect ratio for the entire aspect ratio range shown in Fig. 9 (top left).  
 191 On the other hand, all spanwise nonuniform ( $n > 0$ ) modes are destabilized by an increasing aspect  
 192 ratio. Furthermore, this same figure implies that all spanwise cell patterns become absolutely  
 193 unstable at the same time when  $A \rightarrow \infty$ . The behavior of spanwise nonuniform modes, however, is  
 194 not monotonic with respect to the aspect ratio. At small  $A$ , they are streamwise uniform ( $\text{Re}[k_a] =$   
 195 0), stationary ( $\text{Im}[\lambda_a] = 0$ ) and their spatial growth rates ( $-\text{Im}[k_a]$ ) increase with  $A$ . Beyond a certain

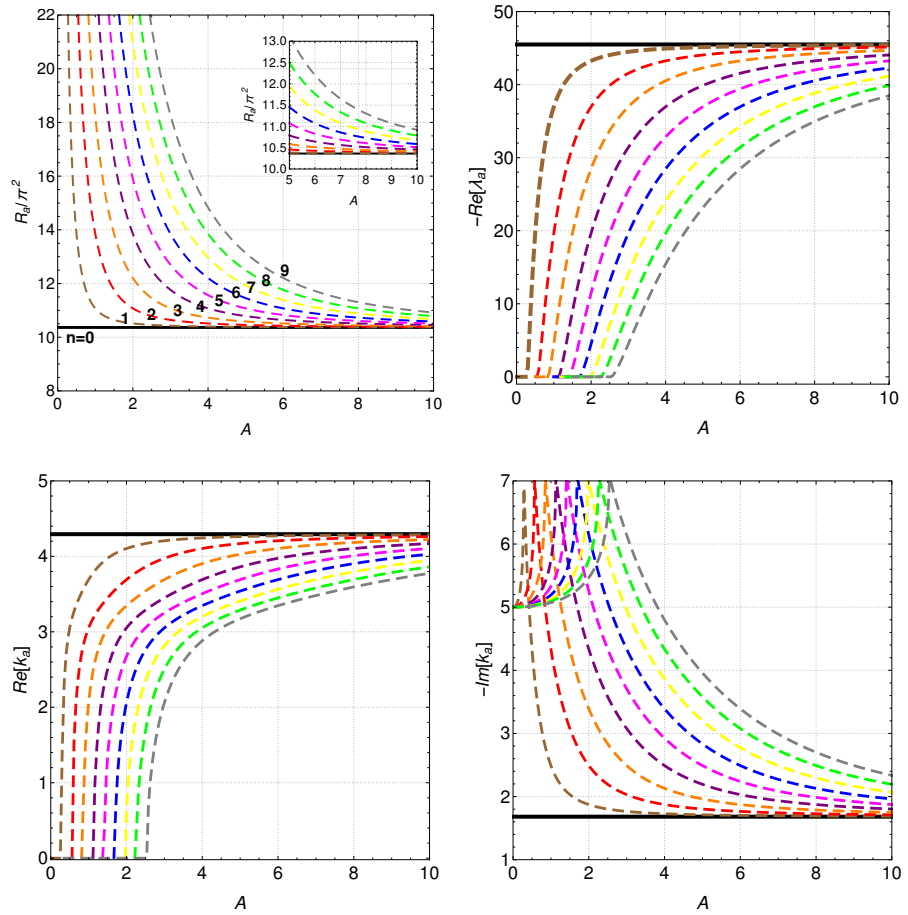


FIG. 9. Absolute critical values to  $Pe = 10$  and  $H = 30$ , considering  $n$  and  $A$  variation.

196 critical aspect ratio, they become streamwise nonuniform ( $\text{Re}[k_a] \neq 0$ ), oscillatory ( $\text{Im}[\lambda_a] \neq 0$ )  
197 and their spatial growth rates ( $-\text{Im}[k_a]$ ) decrease with  $A$ . All three characteristic trends seem to  
198 converge towards their respective spanwise uniform mode ( $n = 0$ ) values when  $A \rightarrow \infty$ .

## 199 V. CONCLUSIONS

200 The present paper investigates mixed convection taking place within metallic foams under lo-  
201 cal thermal non–equilibrium between the solid and the fluid phases. This is done in two major  
202 ways. First, the linear convective/absolute threshold values of the Darcy–Rayleigh number for the  
203 onset of instability are evaluated. Second, the cell pattern selected within each unstable region is  
204 estimated within a linear framework. The following remarks are noteworthy:

- 205 1. Local thermal equilibrium has a stabilizing effect on both onsets of convective and absolute  
206 instability, independently of the Péclet number and aspect ratio;
- 207 2. The number of spanwise cell patterns selected at the onset of convective instability, i.e.  
208 marginal stability, increases with aspect ratio. In the limit of an infinite aspect ratio, all  
209 spanwise cell patterns become linearly convectively unstable at the same time;
- 210 3. The number of spanwise cell patterns selected at marginal stability for a fixed aspect ratio  
211 increases as the local thermal non–equilibrium becomes stronger;
- 212 4. Within convective and absolute instability regions, the uniform spanwise mode is the most  
213 unstable for all aspect ratios and extent of local thermal non–equilibrium.

214 According to the literature<sup>1</sup>, metallic foam heat exchangers operate within  $O(1) < Pr <$   
215  $O(10^2)$  and  $O(1) < Re < O(10^2)$ , where  $Pr$  and  $Re$  are the Prandtl and Reynolds numbers, re-  
216 spectively. This means one can expect  $O(1) < Pe < O(10^4)$ . Although natural convection is  
217 always desirable, heat transfer enhancements due to forced convection are dominant at high Péclet  
218 numbers. Hence, the present results are relevant for small and moderate Péclet numbers. They  
219 indicate that natural convection due to a convective instability is a quite likely scenario for any  $Pe$   
220 but natural convection due to an absolute instability is likely only for small  $Pe$ .

## 221 ACKNOWLEDGMENTS

222 This study was financed in part by the Coordenação de Aperfeiçoamento de Pessoal de Nível  
223 Superior - Brazil (CAPES) - Grant 88881.174085/2018-01. Financial support was also provided  
224 by Ministero dell'Istruzione, dell'Università e della Ricerca (Italy) – Grant PRIN2017F7KZWS.

## 225 DATA AVAILABILITY

226 The data that support the findings of this study are available from the corresponding author  
227 upon reasonable request.

## 228 REFERENCES

- 229 <sup>1</sup>K. Boomsma, D. Poulikakos, and F. Zwick, “Metal foams as compact high performance heat  
230 exchangers,” *Mechanics of materials* **35**, 1161–1176 (2003).
- 231 <sup>2</sup>L. Tianjian, “Ultralight porous metals: from fundamentals to applications,” *Acta Mechanica*  
232 *Sinica* **18**, 457–479 (2002).
- 233 <sup>3</sup>S. Mahjoob and K. Vafai, “A synthesis of fluid and thermal transport models for metal foam heat  
234 exchangers,” *International Journal of Heat and Mass Transfer* **51**, 3701–3711 (2008).
- 235 <sup>4</sup>B. Pulvirenti, M. Celli, and A. Barletta, “Flow and convection in metal foams: A survey and  
236 new CFD results,” *Fluids* **5**, 155 (2020).
- 237 <sup>5</sup>C. W. Horton and F. T. Rogers Jr, “Convection currents in a porous medium,” *Journal of Applied*  
238 *Physics* **16**, 367–370 (1945).
- 239 <sup>6</sup>E. R. Lapwood, “Convection of a fluid in a porous medium,” in *Mathematical Proceedings of*  
240 *the Cambridge Philosophical Society*, Vol. 44 (Cambridge University Press, 1948) pp. 508–521.
- 241 <sup>7</sup>M. Prats, “The effect of horizontal fluid flow on thermally induced convection currents in porous  
242 mediums,” *Journal of geophysical research* **71**, 4835–4838 (1966).
- 243 <sup>8</sup>P. A. Sturrock, “Kinematics of growing waves,” *Physical Review* **112**, 1488 (1958).
- 244 <sup>9</sup>R. Briggs, “Electron–stream interaction with plasmas,” (1964).
- 245 <sup>10</sup>P. Huerre and P. A. Monkewitz, “Absolute and convective instabilities in free shear layers,”  
246 *Journal of Fluid Mechanics* **159**, 151–168 (1985).
- 247 <sup>11</sup>F. Dufour and M.-C. Néel, “Numerical study of instability in a horizontal porous channel with  
248 bottom heating and forced horizontal flow,” *Physics of Fluids* **10**, 2198–2207 (1998).

- 249 <sup>12</sup>M. N. Ouarzazi, A. Joulin, P.-A. Bois, and J. K. Platten, “Soret effect and mixed convection in  
250 porous media,” in *Thermal Nonequilibrium Phenomena in Fluid Mixtures* (Springer, 2002) pp.  
251 428–447.
- 252 <sup>13</sup>A. Delache, M. Ouarzazi, and M. Combarous, “Spatio-temporal stability analysis of mixed  
253 convection flows in porous media heated from below: comparison with experiments,” *International journal of heat and mass transfer* **50**, 1485–1499 (2007).
- 254 <sup>14</sup>L. Brevdo and M. S. Ruderman, “On the convection in a porous medium with inclined tempera-  
255 ture gradient and vertical throughflow. part ii. absolute and convective instabilities, and spatially  
256 amplifying waves,” *Transport in porous media* **80**, 153–172 (2009).
- 257 <sup>15</sup>L. Brevdo, “Three-dimensional absolute and convective instabilities at the onset of convection in  
258 a porous medium with inclined temperature gradient and vertical throughflow,” *Journal of fluid  
259 mechanics* **641**, 475–487 (2009).
- 260 <sup>16</sup>S. da C. Hirata and M. N. Ouarzazi, “Three-dimensional absolute and convective instabilities  
261 in mixed convection of a viscoelastic fluid through a porous medium,” *Physics letters A* **374**,  
262 2661–2666 (2010).
- 263 <sup>17</sup>E. Diaz and L. Brevdo, “Absolute/convective instability dichotomy at the onset of convection  
264 in a porous layer with either horizontal or vertical solutal and inclined thermal gradients, and  
265 horizontal throughflow,” *Journal of fluid mechanics* **681**, 567–596 (2011).
- 266 <sup>18</sup>L. S. de B. Alves and A. Barletta, “Convective to absolute instability transition in the Prats flow  
267 of a power-law fluid,” *International Journal of Thermal Sciences* **94**, 270–282 (2015).
- 268 <sup>19</sup>A. Barletta and L. S. de B. Alves, “Absolute instability: A toy model and an application to the  
269 Rayleigh–Bénard problem with horizontal flow in porous media,” *International Journal of Heat  
270 and Mass Transfer* **104**, 438–455 (2017).
- 271 <sup>20</sup>M. Schuabb, L. S. de B. Alves, and S. da C. Hirata, “Two-and three-dimensional absolute  
272 instabilities in a porous medium with inclined temperature gradient and vertical throughflow,”  
273 *Transport in Porous Media* **132**, 135–155 (2020).
- 274 <sup>21</sup>A. Barletta, *Routes to Absolute Instability in Porous Media* (Springer, 2019).
- 275 <sup>22</sup>M. Combarous, “Description du transfert de chaleur par convection naturelle dans une couche  
276 poreuse horizontale a laide dun coefficient de transfert solidefluide,” *Comptes Rendus Mathé-  
277 matique* **275**, 1375–1378 (1972).
- 278 <sup>23</sup>N. Banu and D. A. S. Rees, “Onset of Darcy–Bénard convection using a thermal non-  
279 equilibrium model,” *International Journal of Heat and Mass Transfer* **45**, 2221–2228 (2002).
- 280

- 281 <sup>24</sup>A. Delache and M. Ouarzazi, “Weakly nonlinear interaction of mixed convection patterns in  
282 porous media heated from below,” *International journal of thermal sciences* **47**, 709–722 (2008).
- 283 <sup>25</sup>B. Bidin and D. A. S. Rees, “Pattern selection for Darcy–Bénard convection with local thermal  
284 nonequilibrium,” *International Journal of Heat and Mass Transfer* **153**, 119539 (2020).
- 285 <sup>26</sup>A. Delache and M. Ouarzazi, “Weakly nonlinear interaction of mixed convection patterns in  
286 porous media heated from below,” *International journal of thermal sciences* **47**, 709–722 (2008).
- 287 <sup>27</sup>P. Huerre and P. A. Monkewitz, “Local and global instabilities in spatially developing flows,”  
288 *Annual Review of Fluid Mechanics* **22**, 473–537 (1990).
- 289 <sup>28</sup>L. S. de B. Alves, S. da C. Hirata, M. Schuabb, and A. Barletta, “Identifying linear absolute  
290 instabilities from differential eigenvalue problems using sensitivity analysis,” *Journal of Fluid*  
291 *Mechanics* **870**, 941–969 (2019).
- 292 <sup>29</sup>A. Barletta, *Routes to Absolute Instability in Porous Media* (Springer, New York, 2019).
- 293 <sup>30</sup>K. Kupfer, A. Bers, and A. K. Ram, “The cusp map in the complex-frequency plane for absolute  
294 instabilities,” *Physics of Fluids* **30**, 3075–3082 (1987).



58 local thermal non-equilibrium on the pattern formation for mixed convection in porous media<sup>11</sup>. In  
 59 the present analysis, however, only the linear pattern selection is discussed. This is accomplished  
 60 by employing the linear growth rates given by both the convective and absolute instability analyses.

## 61 II. PROBLEM STATEMENT

62 A fluid saturated porous layer is bounded horizontally by impermeable and isothermal walls  
 63 and vertically by adiabatic and impermeable walls. This porous channel is subject to a horizontal  
 64 pressure gradient. A vertical temperature gradient is set up by imposing two different temperatures  
 65 at the boundaries with the highest temperature on the lower one. The problem configuration  
 66 coincides with the one investigated by Prats, but with a lateral confinement.  
 67 Among all the possible porous media, we are interested in investigating metallic foams. These  
 68 peculiar, highly conductive, porous media are suitable for designing innovative heat exchangers.  
 69 In this framework, heat transfer processes characterised by fast transients are frequent. In order  
 70 to analyse this type of phenomena, a two-temperature model is here employed: one temperature  
 71 describing the heat transfer for the fluid phase and one temperature for the heat transfer for the solid  
 72 phase. This model allows us to relax the hypothesis of local thermal equilibrium (LTE) between the  
 73 solid phase and the fluid phase.

74

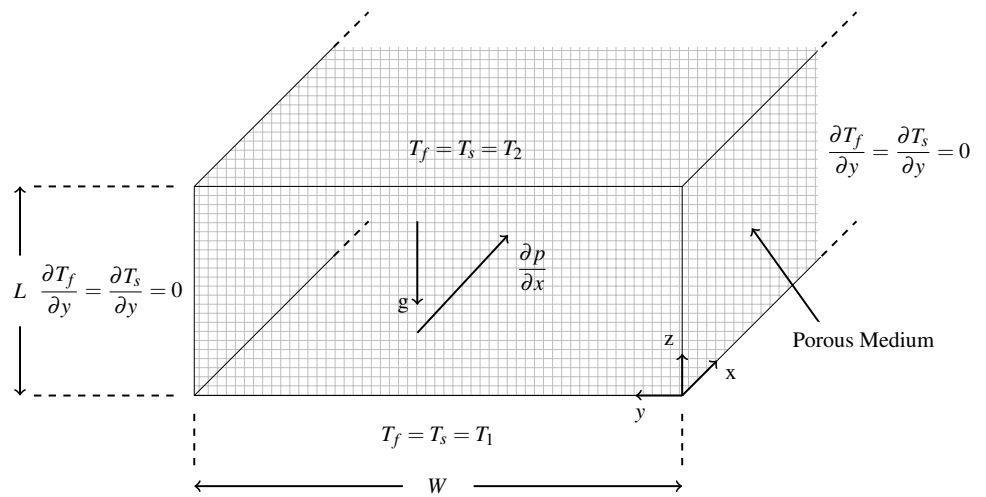


FIG. 1. Problem geometry

